ARTICLE TEMPLATE

Prescribed Grass Fire Evolution Mapping and Rate of Spread Measurement Using Orthorectified Thermal Imagery from a Fixed-Wing UAS

Saket Gowravaram[a], Haiyang Chao[a], Tiebiao Zhao[b], Sheena Parsons[c], Xiaolin Hu[d], Ming Xin[e],Harold Flanagan[a] and Pengzhi Tian[a]

[a]Department of Aerospace Engineering, University of Kansas, Lawrence, KS, USA;
[b]Mechatronics, Embedded Systems and Automation Lab, University of California Merced, CA, USA;
[c]Kansas Biological Survey & Center for Ecological Research, University of Kansas, Lawrence, KS, USA;
[d]Department of Computer Science, Georgia State University, Atlanta, GA USA;
[e]Department of Mechanical and Aerospace Engineering, University of Missouri, Columbia, MO, USA.

ARTICLE HISTORY
Compiled March 24, 2022

ABSTRACT
Fire metrics such as fire front location and rate of spread (ROS) are critical to understanding the behavior of prescribed fires and wildfires. This paper proposes a new method for prescribed grass fire evolution mapping and ROS measurement using multitemporal thermal orthomosaics collected by a small fixed-wing Unmanned Aircraft System (UAS) at low altitudes. The proposed method provides a low-cost, safe, and effective solution for active grass fire monitoring and fire metric measurement in areas that may be challenging for a typical rotor-wing UAS to cover due to endurance and size constraints. The proposed method is demonstrated using a prescribed grass fire data set collected by the KHawk fixed-wing UAS over a 13 ha. Kansas tallgrass prairie field on October 8, 2019. Repeat-pass thermal images collected by the KHawk UAS during about 10 minutes of the burning were grouped and processed to produce multitemporal orthomosaics with a spatial resolution of about 0.23 m and a horizontal position error of about 1.5 m. The resulting orthomosaics were further processed for fire front extraction and the measurement of fire front location and ROS. The head fire ROS of this grass burn was observed to be between 0.2-0.4 ms^{-1} with a mean value of 0.27 ms^{-1}.

KEYWORDS
Unmanned aircraft system (UAS), grass fire monitoring, prescribed grass fire rate of spread, thermal remote sensing, thermal imagery, hazard monitoring.

1. Introduction

Accurate understanding of wildland fire behavior in different environmental and fuel contexts is critical to prescribed fire planning and operation as well as wildfire prevention and mitigation. The fire front location and rate of spread (ROS) are two

Department of Aerospace Engineering, University of Kansas, 2120 Learned Hall, 1530 W 15th St., Lawrence, KS, USA. (E): gnsaket@gmail.com, chaohaiyang@ku.edu.

important fire behavior metrics that are very useful to fire ecology researchers (Bidwell and Engle 1992) interested in understanding the impact of fuel and vegetation on fire evolution, fire modeling researchers (Hu et al. 2021) who may focus on developing accurate fire spread models, and operational fire forecasting researchers (Gollner et al. 2015) interested in building accurate predictive fire models. Many of these above applications often use fire ROS measurements for fire spread modeling and evaluation and therefore, value the accuracy and scale of these measurements over the processing time.

Most remote sensing-based fire location and ROS measurements are performed by post-processing satellite or airborne images acquired during the fire activity. Historically, satellites have been a major source of data for fire mapping, including the detection of active fires and hot spots (Wilfrid et al. 2008; Csiszar, Morisette, and Giglio 2006; Csiszar et al. 2014), fire spread modelling (Coen and Schroeder 2013), and fire damage assessment (Badarinath, Sharma, and Kharol 2011). However, due to coarse spatial resolutions (250 - 1000 m) and slow revisit times (1 day or more), satellite data may not be effective in measuring fire ROS at fine spatial and temporal scales, especially for prescribed fires that are usually completed within hours or wildfires that are contained within a day. Additionally, it is suggested that spatial and temporal resolutions of 10 m and 10 min are desired for reliable data-enabled operational wildfire spread modelling and forecasting (Gollner et al. 2015). This has encouraged the use of other remote sensing sources such as manned aircraft for fire ROS measurements.

Repeat-pass thermal infrared imagery collected by Pacific Southwest Research Station (PSW) FireMapper fire imaging system aboard a manned aircraft were processed post-fire for the measurement and analysis of wildfire ROS in the San Dimas forest in 2002 at a spatial scale of $10^1 - 10^3$ m, which was validated using ground-observations of similar fields from previous literature (Stow et al. 2014). A series of image processing tools were developed for the automatic extraction of fire line parameters including, fire line location and fire front direction using airborne multispectral images and post processed NDVI (Ononye, Vodacek, and Saber 2007). Similarly, airborne imagery from the King Air B200t research aircraft were used for remote measurements of fire intensity, fire line geometry, heat and carbon fluxes during large wildland fires in Brazil (Riggan et al. 2004). Airborne images from the Forestry Services of Castilla-La Mancha were orthorectified post-fire to form fire isochrones which were then used to calculate the fire location and fire ROS for forest fires (Viedma et al. 2015, 2020). In summary, manned aircraft have been successfully used for real-time fire mapping and post-fire ROS measurements since they can collect images with high spatial and temporal resolutions (sub-meter level every few hours). However, they are limited by cost of operation, pilot safety, and limited flexibility in flight path modifications, which has motivated the use of Unmanned Aircraft Systems (UAS) for these applications.

UAS with low-cost multispectral or hyperspectral cameras are generally easier to handle and can fly autonomously over fires without putting human pilots at risk, making them an ideal platform for fire-related applications. However, since they generally fly at low altitudes (mostly $\leq$120 m above ground level in USA due to FAA regulations), fire generated turbulence and smoke can have an impact on their safety and data quality if not well planned (Valero et al. 2021). Although UAS has been used for many wildland fire applications, including vegetation impact mapping (McKenna et al. 2017; Reilly et al. 2021; Samiappan et al. 2019; Fraser, Van der Sluijs, and Hall 2017), fire ignition (Beachly et al. 2017), and fire detection (Yuan, Zhang, and Liu 2015; Gowravaram et al. 2021), its use in fire ROS measurements is still limited in existing

literature. The few UAS-based fire ROS measurements to date have been restricted to small spatial scales (about 1 ha. or less) and hovering multi-rotor UAS likely due to safety concerns for operation in dangerous fire environments. For example, multispectral images from a multi-rotor UAS were used for the estimation of complex fire progression, ROS, and spread direction in prescribed fires, where the UAS was positioned at a fixed location while capturing a fire in a spatial scale of 0.01 - 1 ha (Moran et al. 2019). The use of autonomous fixed-wing UAS for mapping and measurement of fire ROS is lacking, which we aim to address in this paper.

This study introduces a novel method for fire evolution mapping and fire ROS measurement using a small fixed-wing UAS operating at low altitudes above the burning field. The proposed method is demonstrated using a data set collected by a KHawk fixed-wing UAS while observing a prescribed burn of a tallgrass prairie in Anderson County Prairie Preserve, Kansas. The main contributions of this work include:

(1) A new and effective method for accurate recapturing of prescribed grass fire evolution using multitemporal thermal orthomosaics generated by UAS images acquired at low-altitudes.
(2) A UAS thermal data set over a prescribed tallgrass fire in Kansas, which includes the multitemporal thermal orthomosaics and associated weather information (https://cusl.ku.edu/Flight_Log).
(3) Comprehensive measurement, analysis, and validation of fire ROS in a typical tallgrass prairie, which has not been sufficiently addressed in existing remote sensing literature.
(4) Discussions, lessons, and recommendations for safe and efficient operation of small fixed-wing UAS for fire observation.

Through our work, we aim to provide accurate thermal maps and ROS measurements of a tallgrass fire that can be directly used by fire modelling researchers (Hu, Sun, and Ntaimo 2012; Hu et al. 2021) who are interested in understanding grass fires, fire and tallgrass ecologists, land managers, and the prescribed grass fire community. Other UAS and remote sensing researchers can use our methods, lessons learned, and shared data as a resource to develop their systems and to set up future collaborations.

2. Prescribed Fire and Data

This section provides detailed descriptions of the prescribed fire event, including the aerial data collected by a fixed-wing UAS, and wind data collected by a ground weather station during the burn.

2.1. *Prescribed Fire Experiment*

A prescribed grass fire was conducted on October 8, 2019, between 11:38 AM and 12:25 PM (Central Daylight Time (CDT)) at the Anderson County Prairie Preserve, Kansas ($38.183347°, -95.279201°$), shown in Fig. 1. This site is a rectangular grassland field approximately 530 m $\times$ 250 m, relatively flat (1-3 % slope), spanning three soil types (SSURGO Soils: Clareson complex, Wagstaff silty clay loam, Kenoma silt loam) with fine fuel vegetation cover dominated by C4 tallgrasses and a mixture of herbaceous forbs and legumes (shown in Fig. 2). The mean wind during the burn was around 6.26 ms^{-1} from the south based on the ground weather station measurement at $\sim$ 1.9

m above the ground. The ambient temperature was around 73° F while the relative humidity was around 41 %. A small (approx. 0.1 inch) rain event was recorded in the area on October 5, 2019 (Mesonet 2021). This prescribed burn was performed by the Kansas Biological Survey (KBS) for grassland ecosystem management using a ring pattern ignition with two teams starting around the midpoint of the northern boundary (due to south wind). Each team then moved in opposite directions along the boundaries before meeting around the midpoint of the southern boundary. The fire propagated towards the center of the field from all the boundaries.

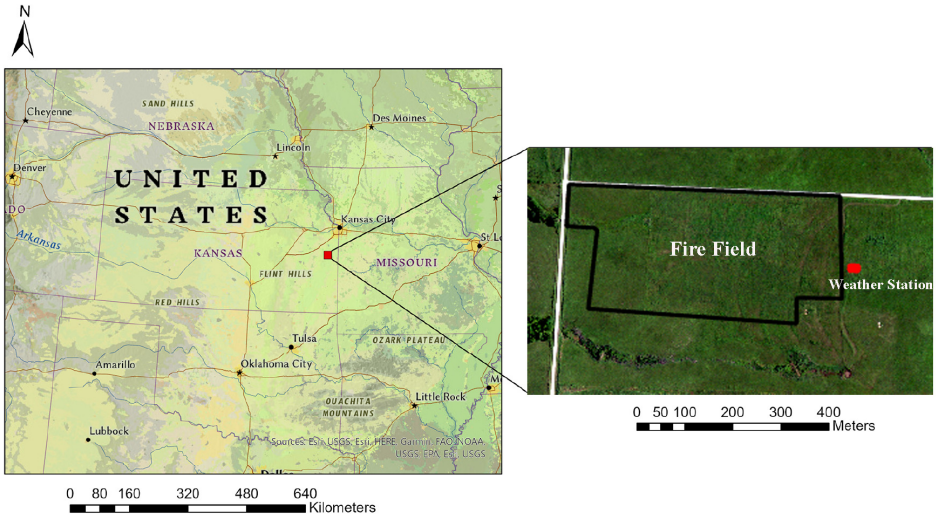

Figure 1. Anderson County Prairie Preserve: fire field (black border) and weather station (red circle) labelled.

Figure 2. Anderson County Prairie Preserve ground picture.

2.2. *KHawk UAS Data*

Thermal remote sensing data was collected by a KHawk 55 thermal fixed-wing UAS during the Anderson County fire. The KHawk 55 thermal UAS is a low-cost multispectral remote sensing platform developed by researchers at the CUSL at the University of Kansas, shown in Fig. 3. It is equipped with a Ublox M8P Here GPS and a Pixhawk

Cube autopilot (ArduPilot 2021) , which can support both manual and autonomous flight. The detailed specifications are provided in Table 1.

Table 1. KHawk 55 Thermal UAS Specifications.

Description	Value
Take-off Weight	2.5 kg
Wingspan	1.4 m
Cruise Speed	20 ms^{-1}
Maximum Endurance	30 min
Typical Altitude	120 m
Spatial Resolution (at 120 m above the ground)	0.23 m

A FLIR Vue Pro R camera is used for thermal image acquisition and its specifications are listed in Table 2. These images were acquired in a 14-bit TIFF format and geotagged real-time through the MAVLink connection with the Pixhawk autopilot.

Table 2. FLIR Vue Pro R Thermal Camera Specifications.

Description	Value
Spectral Bandwidth	7.5 to 13.5 μm
Sensor Resolution	640 × 512 pix
Field-of-View (FOV)	69° × 56°
Frame Rate	1 Hz

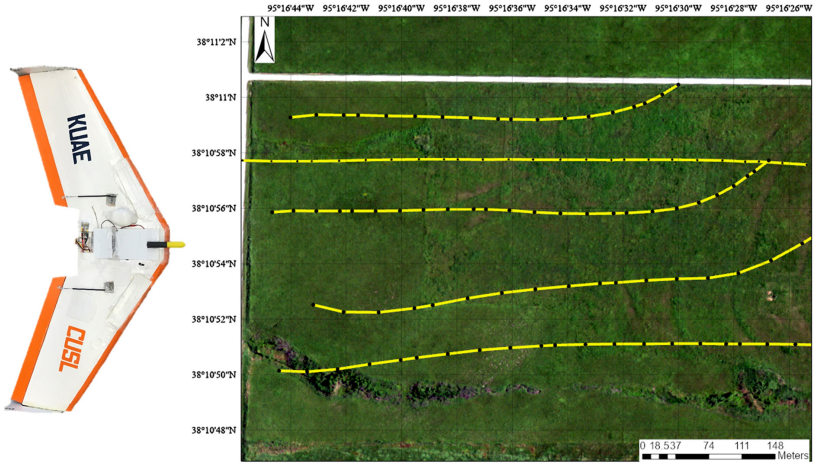

Figure 3. KHawk 55 Thermal UAS (L) and its partial flight path during the fire (R).

The KHawk thermal 55 UAS was deployed and the collected thermal images from 12:06:05 PM to 12:17:47 PM were processed and used in this paper. The UAS was programmed to fly autonomously at around 120 m above the ground to collect repeat-pass time-sequential images which can be used to generate multitemporal orthomosaics. Two pairs of repeat-pass thermal images with their respective time stamps observing the same area are shown in Fig. 4 as an example, where the top images are acquired one second apart from one UAS flight loop and bottom images are from a different

flight loop. The UAS flew multiple loops over the field at an approximate interval of about 2 min such that the set of images captured within each loop can be used to generate one orthomosaic. Only images from straight path with wings level flight are used for orthorectification. The majority of the UAS flight path with effective image acquisition overlaid on a National Agriculture Imagery Program (NAIP) image (spatial resolution of 1 m) is shown in Fig. 3. The NAIP image was used as a reference image for orthomosaic registration, which is further discussed in Sec. 4.1.

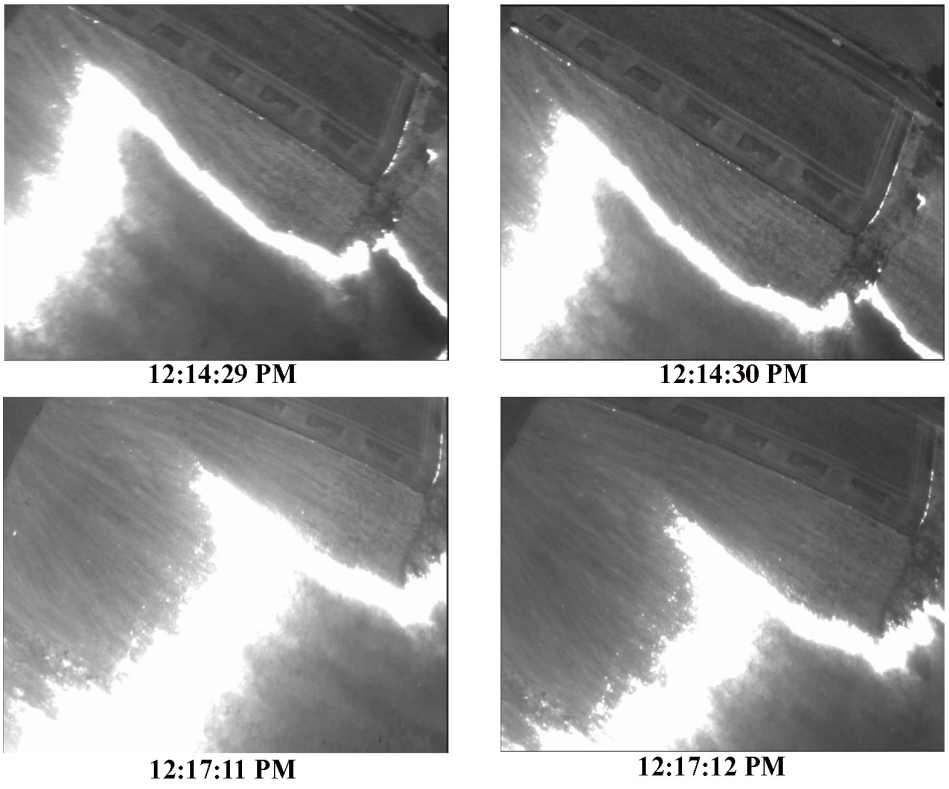

Figure 4. Example KHawk thermal repeat-pass image pairs along the west boundary: top and bottom images are from different UAS flight loops.

2.3. *Ground Wind Measurement Data*

A Campbell Scientific CSAT3B wind anemometer was placed about 20 m east of the eastern boundary (labelled in Fig. 1) at a height of $\sim$ 1.9 m from the ground to measure the 3D wind speed and temperature at an update rate of 100 Hz.

Note that although the fire ignition and burning lasted for about 43 minutes, only 10 min of fire and wind data from 12:06:50 PM to 12:17:47 PM were used for analysis in this paper. This is due to UAS battery constraints, field planning limitation, and safety precautions for UAS operations in close vicinity of fires and fire generated smoke. Fig. 5 shows the measured wind direction and 2D horizontal wind speed (smoothed by a 20-sec moving average filter) during this time. The prevailing wind was from

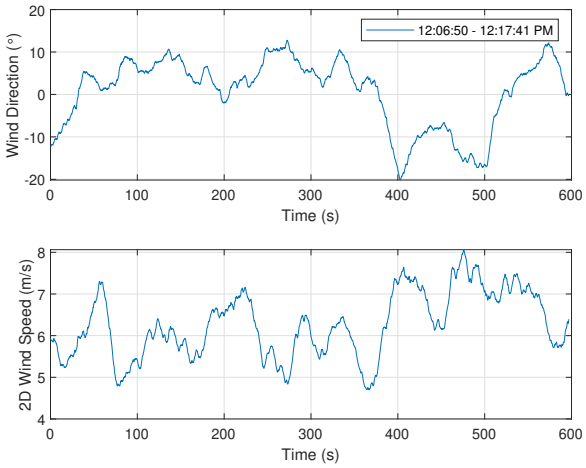

Figure 5. Wind direction and 2D horizontal wind speed between 12:06:50 PM and 12:17:47 PM from Campbell Scientific anemometer.

the south at an average speed of 6.26 ms^{-1} with an exception around 380 seconds (about 12:13:10 PM) when a brief change in direction occurred as the fire front passed the weather station, and caused a temporary change in the local wind direction (see orthorectified images shown in Sec. 4).

3. Methods

A new method is introduced in this section for fixed-wing UAS-based fire evolution mapping and ROS measurement. The proposed method utilizes UAS acquired repeat-pass thermal images to generate multitemporal orthomosaics, which can be used to represent the dynamic evolution of a fire at regular time intervals. The derived fire evolution map can then be used for the ROS calculation at different time stamps and locations. The main components of this method (Fig. 6) include 1) multitemporal orthomosaic generation, 2) fire evolution mapping, and 3) fire ROS calculation.

3.1. *Multitemporal Orthomosaic Generation*

The first step of this method is to generate multitemporal orthomosaics using UAS collected repeat-pass thermal images. Each orthomosaic corresponds to a specific interval of time and is generated using multiple images belonging to a single UAS flight loop. Here, a flight loop is defined as the UAS path that can provide a complete coverage of the field once. These orthomosaics capture the fire evolution at different stages and can be combined to form a fire evolution map. This process can be formulated as below.

Given a UAS flying m loops over a fire field acquiring n geotagged images per loop, $I_b = \{i_{1b}, i_{2b}, ...i_{nb}\}$ with corresponding timestamps, $T_b = \{t_{1b}, t_{2b}, ...t_{nb}\}$, where b refers to the loop index. A total of m orthomosaics, $O_b = \{O_1, O_2....O_m\}$ can be generated by georeferencing and stitching all the images corresponding to each loop as

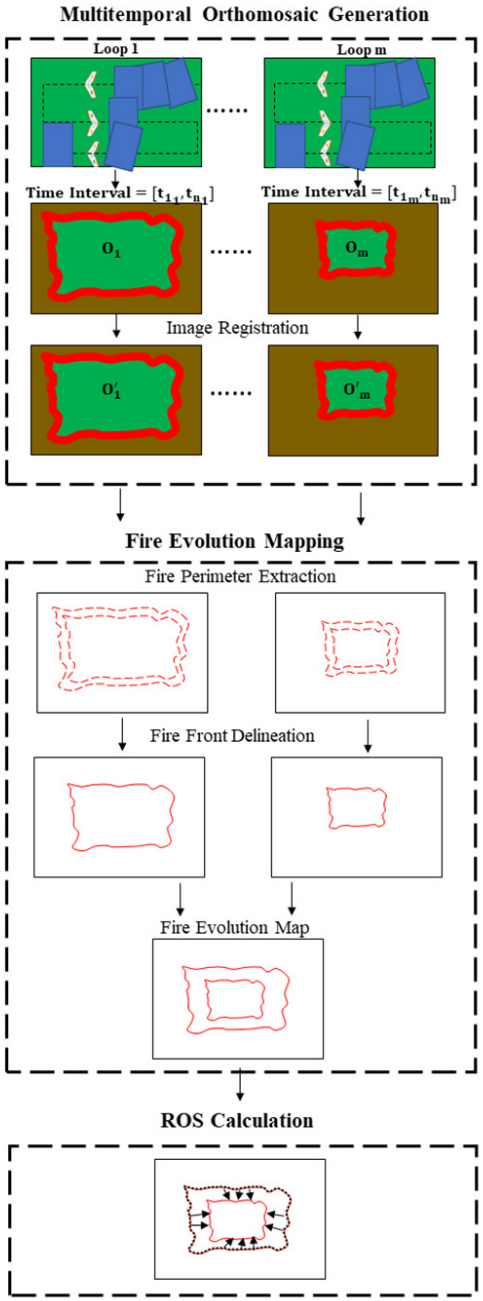

Figure 6. Flow diagram for fixed-wing UAS-based fire evolution mapping and ROS calculation.

shown below.

$$\begin{aligned} I_1 &= \{i_{11}, i_{21}, ...i_{n1}\} \rightarrow O_1 \\ I_2 &= \{i_{12}, i_{22}, ...i_{n2}\} \rightarrow O_2 \\ &\cdot \\ I_m &= \{i_{1m}, i_{2m}, ...i_{nm}\} \rightarrow O_m \end{aligned} \tag{1}$$

Each orthomosaic, O_b contains information from n images with n timestamps from t_{1b} to t_{nb}. Generation of such orthomosaics is illustrated in the top block of Fig. 6. Due to possible spatial uncertainties and misalignments, each orthomosaic is recommended to be registered with a high-accuracy reference image before they are used for any fire metric measurements.

3.2. *Fire Evolution Mapping*

Registered orthomosaics can be used to generate a fire evolution map that contains multiple fire fronts from each orthomosaic using two steps, 1) fire perimeter extraction and 2) fire front delineation. The fire perimeter, f' is defined as the entire outer edge of a fire (USDA 2021), including the leading and trailing edges, where the leading edge represents the fire front. The fire perimeter can be extracted from a thermal orthomosaic using temperature or intensity-based thresholds as shown below.

$$f'_b = \begin{cases} 1, & \text{if } O'_b \geq \alpha \\ 0, & \text{otherwise,} \end{cases} \tag{2}$$

where α is a temperature or intensity-based threshold.

The extracted fire perimeter is usually in the form of discrete points, which is not desirable for further fire ROS spread vector determination. The next step is to delineate fire fronts, f_b from each orthomosaic, where continuous curves are created from discrete pixels along the leading edge of the fire perimeter, f'_b. A manual delineation procedure can be used to connect these discrete pixels to result in continuous fire fronts (Stow et al. 2019). The final delineated fire fronts corresponding to each orthomosaic can be added to form the fire evolution map, F, such that $F = f_1 + f_2 .... + f_m$. An illustration of the fire evolution mapping procedure for orthomosaics O_1 and O_m is shown in the middle block of Fig. 6.

3.3. *ROS Measurement*

The final step of this method is the fire ROS calculation. The calculation of fire ROS between consecutive fire fronts, f_b and f_{b+1}, requires the distance and time-lapsed between them. First, p equally-spaced points are selected such that $f_b = \{A_1, A_2, ...A_p\}$, where A_p is the location of the pth point along f_b.

Next, the spread vectors, $\vec{AB}$ can be drawn along the direction perpendicular to the local curve from A_p until they intersect the consecutive fire front at B along f_{b+1}. Note that other approaches for fire spread vector determination exist in the literature including drawing the vector along the visual and wind direction trends, however, no substantial differences were observed between these different approaches (Stow et al. 2019). Finally, the time interval between the individual images ΔT can be calculated. The ROS can be calculated using the following equation.

$$ROS_A = \frac{\|\vec{AB}\|}{\Delta T} \tag{3}$$

The bottom part of Fig. 6 illustrates the ROS calculation between two fire fronts corresponding to orthomosaics I_1 and I_m.

4. Results

The proposed method is implemented and validated using the Anderson County fire data set and corresponding results are presented in this section.

4.1. *Multitemporal Orthomosaic Generation*

Repeat-pass thermal images collected by the KHawk thermal UAS from 12:06:50 PM to 12:17:47 PM are used to generate four multitemporal orthomosaics (O_1,O_2,O_3,O_4), as shown in Fig. 7. The Agisoft Photoscan Pro software was used for the orthorectification process. It is known that orthorectifying thermal images can be challenging due to low image resolution and contrast in the thermal band (Yang and Lee 2019). To overcome this challenge, the FLIR Vue Pro R camera was set at the 14-bit tiff mode such that the resulting images had the least compression and highest radiometric resolution. Additionally, since these thermal images contained fire pixels, there was a sufficient contrast for feature matching. Therefore, the overall process for the thermal orthomosaic generation in the Agisoft Photoscan software was similar to that of RGB images. Each orthomosaic covers the same area at spatial scales of order 10^4 m^2 with a temporal resolution about two minutes. Important properties including number of images used and time-interval for each orthomosaic are listed in Table 3. Note that not all the images within the start-end time frame were used for stitching and some images were manually excluded due to blurriness or when the UAS was not flying straight and wings-level. O_2 (top right) has some stitching errors due to a few improperly aligned images in areas where the fire is not present, caused mainly by slow and inaccurate UAS flight path adjustments during the burn.

Table 3. Multitemporal Thermal Orthomosaic Properties.

Orthomosaic	Number of Images	Start-End Time (CDT)
O_1	119	$12:06:50 - 12:09:18$ PM
O_2	103	$12:09:34 - 12:10:44$ PM
O_3	96	$12:12:41 - 12:15:02$ PM
O_4	85	$12:15:27 - 12:17:47$ PM

The generated orthomosaics are co-registered with a NAIP image with a spatial resolution of 1 m using the ArcGIS Georeferencing tool. The NAIP image was acquired on June 30, 2019 and has a horizontal position accuracy of about 6 m at a confidence level of 95% (USDA 2009). Multiple control point pairs are manually selected from each KHawk orthomosaic and the NAIP image such that they are spread out across the whole field. Table 4 shows the registration attributes for each orthomosaic where the registration errors for all the orthomosaics are at similar levels (about 1.5 m). Another observation is that only 5 and 7 control point pairs are used for O_2 and O_4 as compared to 10 pairs for the other two. This is because the images from the UAS flight loop used for O_2 were not very stable due to turbulence experienced by the UAS and caused some stitching errors. The fire and its surrounding regions (smoke, hot regions, etc.) occupy a large portion of the field in O_4 preventing the visibility of many feature points (can be seen in the top and bottom right of Fig. 7).

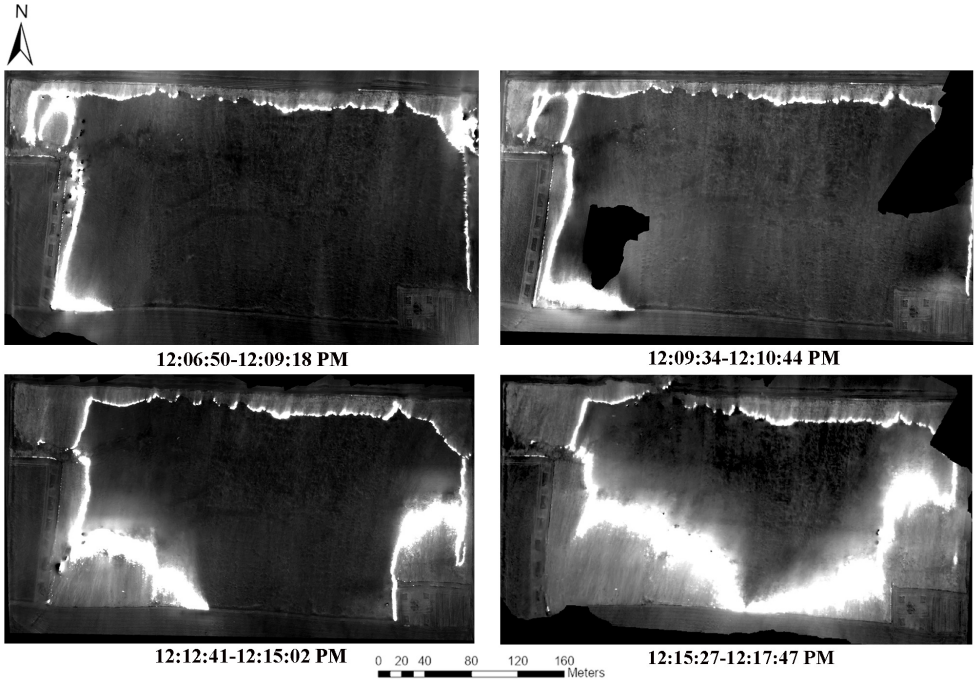

Figure 7. Multitemporal thermal orthomosaics: O_1 (top left), O_2 (top right), O_3 (bottom left), and O_4 (bottom right).

Table 4. Image-to-Image Registration Attributes for Multitemporal Thermal Orthomosaics Using 1 m NAIP Imagery.

Orthomosaic	Spatial Resolution (m)	Control Point Pairs	Transformation Type	RMSE (m)
O_1	0.23	10	Affine	1.32
O_2	0.23	5	Affine	1.59
O_3	0.23	10	Affine	1.49
O_4	0.23	7	Affine	1.52

4.2. *Fire Evolution Mapping*

The fire perimeter is extracted from all the orthomosaics using the standard deviation data classification method in ArcGIS Pro. With class breaks set at one-third of the standard deviation of each orthomosaic, the range of values corresponding to the fire perimeter is determined through visual inspection. It is found that in all the orthomosaics, the fire perimeter pixel values are around 90% of the maximum intensity pixel value in the orthomosaic. Fig. 8 shows the fire perimeter extracted from each orthomosaic.

The fire front isolated from each orthomosaic corresponds to the time interval associated with that orthomosaic (Table 3). The delineated fire fronts are combined into one image, called the fire evolution map, shown in Fig. 9. Here, fire fronts from each orthomosaic are shown in different colors and their corresponding time-intervals are labelled. It is worth mentioning that the time-intervals of these fire fronts are subsets of time-intervals associated with their corresponding orthomosaics. The arrows in this figure represent spread vectors, which are discussed in more detail in the next subsection. The absence of fire fronts along the northern boundary during this time series is

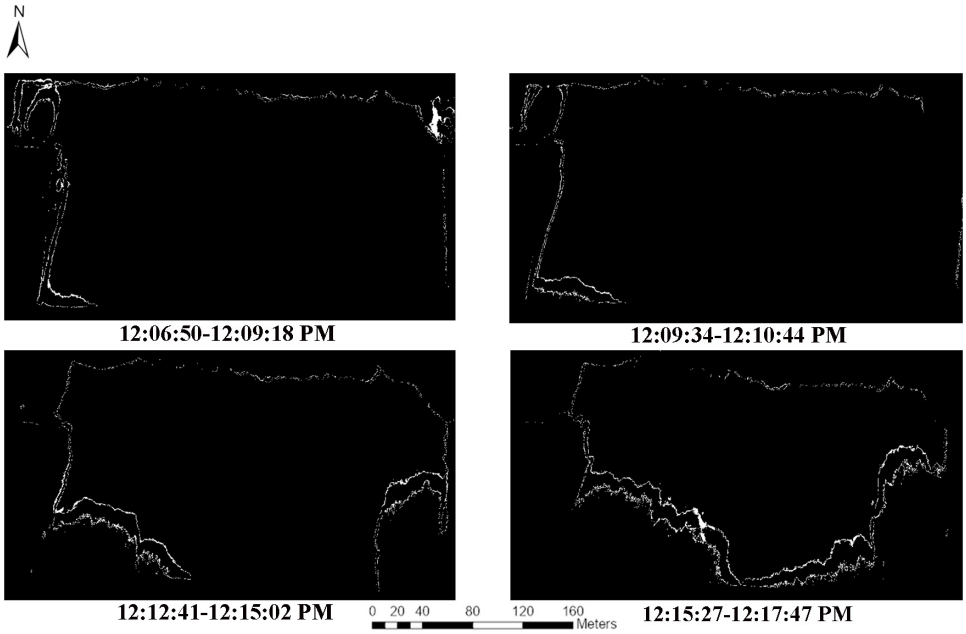

Figure 8. Extracted fire perimeter from multitemporal thermal orthomosaics: f_1' (top left), f_2' (top right), f_3' (bottom left), and f_4' (bottom right).

due to the strong prevailing south wind.

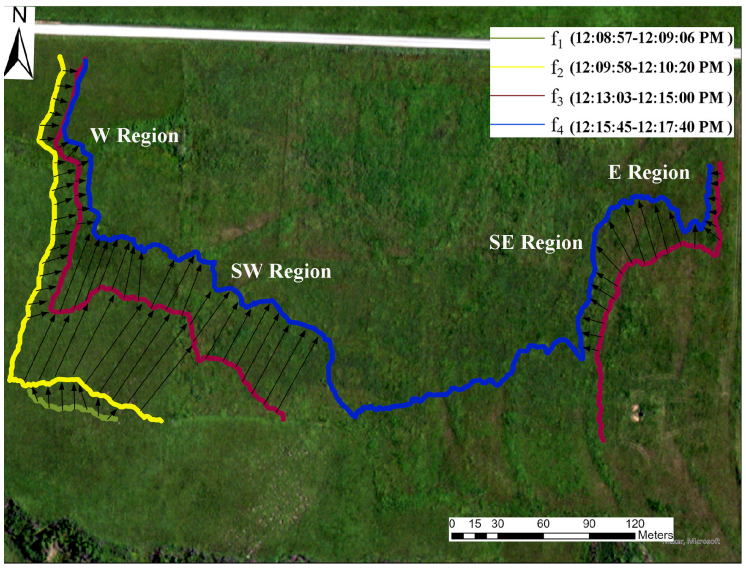

Figure 9. Fire evolution map.

4.3. *ROS Measurement*

Equally-spaced sample points (every 10 m) are selected along each delineated fire front to calculate the ROS. Then spread vectors are drawn from them in the direction of the local normal to the curve, f_b and are extended until they intersect the consecutive fire front, f_{b+1}. These vectors depict the direction of fire spread from each point. The distance between the starting and ending points of the spread vector can then be calculated and used in the ROS calculation for a given point in f_b. Note that the vectors may need to be manually adjusted for cases where two or more vectors intersect or collide. This could occur as a direct consequence of the manual delineation when spread vectors from f_b are drawn in opposite directions or point to the same location in f_{b+1}. The ROS for each point is calculated by dividing the distance by the time-lapsed between them. The time-lapsed is calculated by subtracting the timestamps corresponding to individual images respectively.

The obtained fire ROS measurements are analyzed statistically in different regions based on the location and the fire spread direction. These regions include West (fire spread towards the east), South West (fire spread towards the north/north east), South East (fire spread towards the north/north west), and East (fire spread towards the west). These spread directions are mostly influenced by the prevailing wind direction (from south to north from Fig. 5) and the fire ignition sequence (ring-fire pattern starting from the northern boundary), since the study area is relatively flat with a uniform fuel load. The fire fronts from each map intersect the southern boundary at different locations, indicating that the fire setting is still in progress (Fig. 9).

The ROS measurements in the divided subgroups are visualized in polar plots, shown in Fig. 10. The statistics are further shown in Table 6-8, where the ROS in the South West and South East boundaries have a mean value of 0.26 ms^{-1} and 0.28 ms^{-1} respectively. These values are substantially higher than the West and East boundaries whose mean ROS values are observed to be 0.06 ms^{-1} and 0.11 ms^{-1}. The maximum ROS is found to be 0.4 ms^{-1} in the South West region. Given the wind direction (mostly south to north) and these observed trends, the fire front from the southern boundary can be treated as the head fire while the fire fronts from the east and west can be treated as the flank fire. Based on the analysis shown in this section, the mean head fire ROS is found to be 0.27 ms^{-1} which falls within the ROS range observed in similar tallgrass prairies in north central Oklahoma (Bidwell and Engle 1992).

Table 5. ROS Statistics in the West Region.

Average Lapsed Time	ROS Statistics (ms^{-1})			
	Min	Mean	Max	Std
f_2-f_3 (178.3 s)	0.05	0.08	0.1	0.01
f_3-f_4 (163 s)	0	0.03	0.07	0.02
Cumulative				
	0	0.06	0.1	0.03

4.4. *ROS Uncertainty Analysis*

The objective of this subsection is to estimate the accuracy of the fire ROS calculated in Sec. 4.3. The ROS measurement accuracy mainly depends on the spatial and temporal uncertainties in the multitemporal orthomosaics, as shown in (3). These factors are

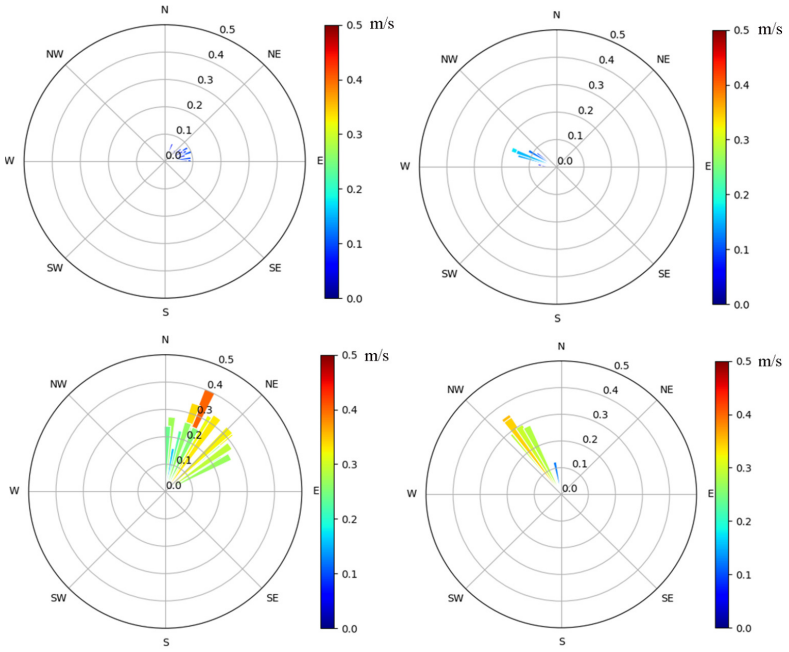

Figure 10. ROS in W (top left), E (top right), SW (bottom left), and SE (bottom right) regions.

Table 6. ROS Statistics in the South West Region.

Average Lapsed Time	ROS Statistics (ms^{-1})			
	Min	Mean	Max	Std
f_1-f_2 (80.8 s)	0.18	0.25	0.32	0.05
f_2-f_3 (269.4 s)	0.16	0.22	0.26	0.04
f_3-f_4 (140.8 s)	0.23	0.28	0.4	0.04
Cumulative				
	0.16	0.26	0.4	0.06

Table 7. ROS Statistics in the South East Region.

Average Lapsed Time	ROS Statistics (ms^{-1})			
	Min	Mean	Max	Std
f_3-f_4 (118 s)	0.12	0.28	0.35	0.07

Table 8. ROS Statistics in the East Region.

Average Lapsed Time	ROS Statistics (ms^{-1})			
	Min	Mean	Max	Std
f_3-f_4 (178 s)	0.04	0.11	0.17	0.05

discussed below.

(1) Time uncertainty of the images: Each multitemporal orthomosaic is generated using n images, each having its own timestamp. The main source of uncertainty

comes from the selection of specific individual images corresponding to the starting and ending of the fire spread vector between consecutive fire fronts. In this paper, a time accuracy of ± 1 second was observed for the fire ROS calculation since the FLIR camera was set to sample at 1 Hz. This has a trivial impact on the final ROS calculation because the time difference between any two fire fronts were around or more than 120 seconds.

(2) Spatial uncertainty of the multitemporal orthomosaics: The ROS is directly influenced by the spatial uncertainties of the multitemporal orthomosaics. For example, given a horizontal position error of δX for each of the consecutive orthomosaics, the ROS during a time interval ΔT can vary as much as $\frac{2\delta x}{\Delta T}$. Given the δX of about 1.5 m (Table 4) for these thermal orthomosaics and an assumed ΔT of about 120 seconds between consecutive fire fronts, the ROS uncertainty can be calculated as $\pm 0.025 ms^{-1}$, which is about 9 % of the mean head fire ROS.

In addition to the above uncertainty analysis, a further validation is conducted using a different fire observation video from a DJI Phantom. This DJI Phantom quadrotor equipped with an RGB camera was launched at 12:20:28 PM (approximately 168 seconds after the last KHawk fixed-wing view of the fire for continuous aerial observation) and manually operated over the north east boundary of the fire field. The fire evolution observed by the DJI at 12:22:03 PM and 12:23:42 PM is shown in Fig. 11. From this figure, fire spread predominantly from the south to the north before consuming the entire field can be observed, confirming the head fire in f_4 travelled a south to north trajectory shown in blue in Fig. 9.

Figure 11. Fire observations from DJI Phantom RGB video with time stamps in CDT.

For the quantitative validation, a fire front, f_{DJI} is extracted from a manually registered DJI image at 12:22:03 PM (left frame in Fig. 11 before registration) and is used as a ground truth to validate the ROS of the head fire calculated in Sec. 4.3. The extracted fire front after registration is shown as the red curve in Fig. 12, which shows the head fire evolution from f_4 and DJI fire front f_{DJI} overlaid on the NAIP image. The objective of this analysis is to compare the calculated mean head fire ROS of 0.27 ms^{-1} and the ROS derived between the f_4 head fire at 12:17:32 PM and the f_{DJI} at 12:22:03 PM. It is worth mentioning that the DJI frame at 12:22:03 PM was selected due to the availability of landmarks in the image FOV.

This analysis supports that the head fire in f_4 would reach f_{DJI} at the expected time if it evolved at a ROS of 0.26 ms^{-1}, which is 0.01 ms^{-1} less than the calculated mean head fire ROS. This error falls within the calculated uncertainty window. Further

anecdotal validation was given by the KBS prescribed fire crew, who confirm that the fire in the area between f_3 and f_{DJI} would be expected to evolve with a fairly constant ROS given the uniform fuel loads, wind and slope distributions at that location during the described burn event.

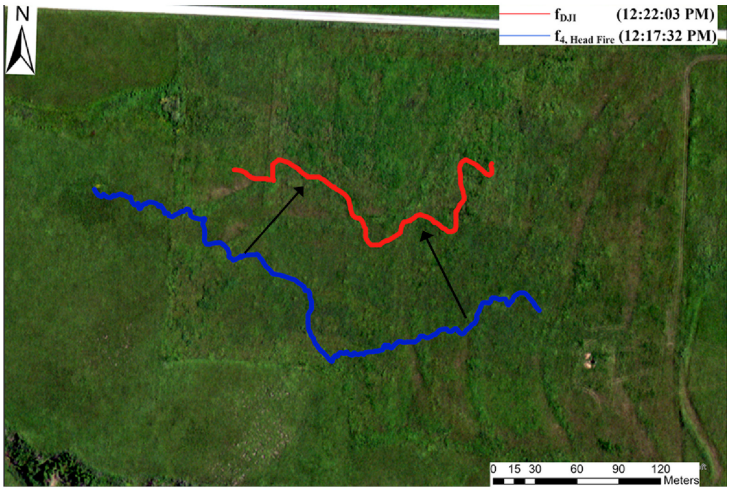

Figure 12. ROS validation: fire evolution between head fire from f_4 and f_{DJI} (from left frame in Fig. 11).

5. Discussions and Recommendations

The effectiveness of the proposed method is dependent on several factors from the UAS path planning to the final ROS calculation. Some of these critical factors are discussed in this section.

5.1. *Fixed-Wing UAS Mission Design for Fire Observation*

Fast evolving processes like fires pose special challenges for fixed-wing UAS based remote sensing because the environment constantly changes spatially and temporally. To monitor such processes, the UAS has to fly multiple loops over the same field at regular time intervals for repeat-pass image acquisition, assuming that the FOV of the UAS camera cannot cover the whole field. During this prescribed fire experiment, the fixed-wing KHawk 55 thermal UAS was programmed to fly an adjustable racetrack type flight pattern with decreasing sizes over time based on prior knowledge and human ground observation of the fire evolution. The work presented in this paper lays a good foundation for future fixed-wing UAS missions for autonomous fire monitoring and real-time fire metric measurements. Based on lessons learned in this paper, the following recommendations are provided for more effective fixed-wing UAS path planning for fire evolution mapping and ROS measurements.

(1) UAS cruise altitude: The UAS flight altitude needs to be carefully selected to reduce the impact of the fire-generated turbulence and smoke on the image quality. In this paper, the KHawk UAS was flown at 120 m above ground such

that it was not heavily impacted by fire-generated turbulence or smoke. This was partially due to strong winds ($\sim 6\ ms^{-1}$ from south) which blew away most of the smoke from the UAS flight path directly above the fire.

(2) UAS flight path: Cross-wind flight path is suggested on windy day, such that the UAS ground speed can be maintained throughout the mission for image acquisition at a constant spatial sampling distance.

(3) UAS flight loops: The UAS needs to cover the study area repeatedly at regular time intervals. It is highly recommended that the UAS flies wings-level and straight over the study area for high-quality image collection and accurate image orthorectification. The UAS can turn outside the perimeter of the fire field and return to a stable and wings-level condition as it covers the fire.

(4) Longitudinal and Lateral image overlapping constraint: Maintaining a desirable longitudinal and lateral overlapping percentages between images is important for the accurate georeferencing and orthorectification. The Agisoft Photoscan Pro software recommends a minimum of 60 % and 70 % for longitudinal and lateral directions respectively. Satisfying these requirements can be challenging due to limited availability of real-time fire information and safety precautions for the UAS. The effect of sub-optimal lateral overlapping can be seen in O_2 (the top right of Fig. 7). The images used to stitch this orthomosaic had less lateral overlapping (< 70 %) near the bottom left and top right areas (holes can be seen in these areas) which impacted the quality of the orthomosaic. This is due to limited real-time fire information and ineffective path planning during the fire burning.

5.2. *Effect of the Camera and Image Processing on Fire Evolution Mapping*

The accuracy of the derived fire evolution map is highly affected by the imaging sensor and its associated image processing techniques. For fire observation, thermal images are highly preferred due to its ability, 1) to see through smoke and 2) easily differentiate fire regions and hot spots from the surroundings. In this study, we observed that the selected FLIR thermal camera provides high-quality data for fire evolution mapping and ROS measurement of tallgrass prescribed fires.

Unlike a general orthorectification process, which georeferences a set of images and stitches them, the multitemporal orthomosaic generation method first segregates the images into different groups based on the time they were acquired and then performs georeferencing and orthorectification for each group separately. Selection of these groups can be critical to the accuracy of the resulting orthomosaics, since the fire is constantly evolving. The fire observed by the KHawk UAS remained about the same along the longitudinal direction within a few seconds but changed along the lateral direction in between two flight lines, which can cause some errors in the orthomosaics. To minimize this problem, multiple images within one group that contain the fire at the same location need to be excluded from stitching. Additionally, images are recommended to be stable (no blurring) and nadir-facing for better spatial and stitching accuracy and quality, which can be challenging for some UAS data due to possible fire-generated turbulence. The orthomosaics shown in Fig. 7 are generated by careful selection and manual removal of images during each stitching process (Table 3).

6. Conclusions & Future Goals

This paper described a low-cost, safe, and efficient method for fire evolution mapping and ROS calculation using thermal imagery collected by a fixed-wing UAS. The method was demonstrated using the KHawk UAS repeat-pass thermal images of a prescribed fire (530 m $\times$ 250 m) in Anderson County, Kansas, where the fire evolution map and associated fire ROS were calculated using four multitemporal orthomosaics at regular time intervals (about 2 minutes). The head fire ROS was observed to be within the range of 0.2-0.4 ms^{-1} with a mean of 0.27 ms^{-1}. Based on our knowledge, this paper provides the first remote sensing based measurement of fire ROS in tallgrass prairie in the Midwest USA. Therefore, the derived fire ROS statistics can serve as a useful reference for future prescribed and wildfires in similar grasslands.

Future goals for fixed-wing UAS based fire evolution mapping and ROS measurement include, 1) near real-time fire map generation, ROS measurement, and data transfer for fire situation awareness, 2) real-time UAS path adjustments based on fire spread behavior, 3) machine learning-based automatic fire front delineation, and 4) integration of cm-level RTK GPS on-board the UAS and use of ground control point (GCP) for improved orthorectification.

Acknowledgment

The authors would like to thank the two anonymous reviewers for providing insightful comments that have helped improve this paper. The authors would also like to thank Dr. Dean Kettle, Bruce Johanning, and Vaughn Salisbury from Kansas Biological Survey for their help with fire experiments and UAS data collection. The authors would like to thank Dr. Walter Fick from Kansas State University and Bryce Haverkamp from the Kansas Forest Service for providing their expert opinions that has benefited this paper. This work is supported in part by the US Department of Agriculture (USDA) National Institute of Food and Agriculture (NIFA) under grant number 2019-67021-29011, 2019-67021-28992, and 2019-67021-28993.

References

ArduPilot. 2021. "The Cube." Digital media. [Available online at https://ardupilot.org/copter/docs/common-thecube-overview.html.].

Badarinath, K.V.S., AR Sharma, and SK Kharol. 2011. "Forest fire monitoring and burnt area mapping using satellite data: a study over the forest region of Kerala State, India." *International Journal of Remote Sensing* 32 (1): 85–102.

Beachly, E., C. Detweiler, S. Elbaum, D. Twidwell, and B. Duncan. 2017. "UAS-Rx interface for mission planning, fire tracking, fire ignition, and real-time updating." In *2017 IEEE International Symposium on Safety, Security and Rescue Robotics (SSRR)*, 67–74. IEEE.

Bidwell, T.G., and D.M. Engle. 1992. "Relationship of fire behavior to tallgrass prairie herbage production." *Rangeland Ecology & Management/Journal of Range Management Archives* 45 (6): 579–584.

Coen, J.L., and W. Schroeder. 2013. "Use of spatially refined satellite remote sensing fire detection data to initialize and evaluate coupled weather-wildfire growth model simulations." *Geophysical Research Letters* 40 (20): 5536–5541.

Csiszar, I.A., J.T. Morisette, and L. Giglio. 2006. "Validation of active fire detection from

moderate-resolution satellite sensors: the MODIS example in northern eurasia." *IEEE Transactions on Geoscience and Remote Sensing* 44 (7): 1757–1764.

Csiszar, I.A., W. Schroeder, L. Giglio, E. Ellicott, K.P. Vadrevu, C.O. Justice, and B. Wind. 2014. "Active fires from the Suomi NPP Visible Infrared Imaging Radiometer Suite: Product status and first evaluation results." *Journal of Geophysical Research: Atmospheres* 119 (2): 803–816.

Fraser, R.H., J. Van der Sluijs, and R.J. Hall. 2017. "Calibrating satellite-based indices of burn severity from UAV-derived metrics of a burned boreal forest in NWT, Canada." *Remote Sensing* 9 (3): 279.

Gollner, M., A. Trouve, I. Altintas, J. Block, R. de Callafon, C. Clements, A. Cortes, et al. 2015. *Towards data-driven operational wildfire spread modeling: A report of the NSF-funded WIFIRE workshop*. Technical Report.

Gowravaram, S., H. Chao, H. Flanagan, P. Tian, J. Goyer, M. Xin, and X. Hu. 2021. "Wildland Fire Monitoring and Mapping Using Orthorectified Near-Infrared and Thermal UAS Imagery." In *American Meteorological Society Annual Meeting, 2021.*, AMS.

Hu, X., M. Ge, S. Gowravaram, H. Chao, and M. Xin. 2021. "Simulating Prescribed Fire with Multiple Ignitions using Data from UAS-based Sensing." *Submitted under Review* .

Hu, X., Y. Sun, and L. Ntaimo. 2012. "DEVS-FIRE: design and application of formal discrete event wildfire spread and suppression models." *Simulation* 88 (3): 259–279.

McKenna, P., P.D. Erskine, A.M. Lechner, and S. Phinn. 2017. "Measuring fire severity using UAV imagery in semi-arid central Queensland, Australia." *International Journal of Remote Sensing* 38 (14): 4244–4264.

Mesonet. 2021. "Iowa Environmental Mesonet." Digital media. [Available online at https://mesonet.agron.iastate.edu/sites/obhistory.php?station=OWInetwork=KS$_A SOS metar = 0 madis = 0 year = 2019 month = 10 day = 8 sortdir = asc$.].

Moran, C.J., C.A. Seielstad, M.R. Cunningham, V. Hoff, R.A. Parsons, L. Queen, K. Sauerbrey, and T. Wallace. 2019. "Deriving fire behavior metrics from UAS imagery." *Fire* 2 (2): 36.

Ononye, A.E., A. Vodacek, and E. Saber. 2007. "Automated extraction of fire line parameters from multispectral infrared images." *Remote Sensing of Environment* 108 (2): 179–188.

Reilly, S., M.L. Clark, L. P. Bentley, C. Matley, E. Piazza, and I. Oliveras Menor. 2021. "The Potential of Multispectral Imagery and 3D Point Clouds from Unoccupied Aerial Systems (UAS) for Monitoring Forest Structure and the Impacts of Wildfire in Mediterranean-Climate Forests." *Remote Sensing* 13 (19): 3810.

Riggan, P.J., R.G. Tissell, R.N. Lockwood, J.A. Brass, J.A. Pereira, H.S. Miranda, A.C. Miranda, T. Campos, and R. Higgins. 2004. "Remote measurement of energy and carbon flux from wildfires in Brazil." *Ecological Applications* 14 (3): 855–872.

Samiappan, S., L. Hathcock, G. Turnage, C. McCraine, J. Pitchford, and R. Moorhead. 2019. "Remote sensing of wildfire using a small unmanned aerial system: post-fire mapping, vegetation recovery and damage analysis in Grand Bay, Mississippi/Alabama, USA." *Drones* 3 (2): 43.

Stow, D.A., P.J Riggan, G. Schag, W. Brewer, R. Tissell, J. Coen, and E. Storey. 2019. "Assessing uncertainty and demonstrating potential for estimating fire rate of spread at landscape scales based on time sequential airborne thermal infrared imaging." *International Journal of Remote Sensing* 40 (13): 4876–4897.

Stow, D.A., P.J. Riggan, E.J. Storey, and L.L. Coulter. 2014. "Measuring fire spread rates from repeat pass airborne thermal infrared imagery." *Remote sensing letters* 5 (9): 803–812.

USDA. 2009. "National Agriculture Imagery Program." Digital media. [Available online at https://www.fsa.usda.gov.].

USDA. 2021. "Fire Terminology." Digital media. [Available online at https://www.fs.fed.us/nwacfire/home/terminology.html.].

Valero, M.M., S. Verstockt, B. Butler, D. Jimenez, O. Rios, C. Mata, L. Queen, E. Pastor, and E. Planas. 2021. "Thermal Infrared Video Stabilization for Aerial Monitoring of Active Wildfires." *IEEE Journal of Selected Topics in Applied Earth Observations and Remote Sensing* 14: 2817–2832.

Viedma, O., F. Chico, J.J. Fernández, C. Madrigal, H.D. Safford, and J. M. Moreno. 2020. "Disentangling the role of prefire vegetation vs. burning conditions on fire severity in a large forest fire in SE Spain." *Remote Sensing of Environment* 247: 111891.

Viedma, O., J. Quesada, I. Torres, A. De Santis, and J. Moreno. 2015. "Fire severity in a large fire in a Pinus pinaster forest is highly predictable from burning conditions, stand structure, and topography." *Ecosystems* 18 (2): 237–250.

Wilfrid, S., P. Elaine, G. Louis, C. Ivan, S. Christopher, M. Jeffrey, and M. Douglas. 2008. "Validation of GOES and MODIS active fire detection products using ASTER and ETM+ data." *Remote Sensing of Environment* 112 (5): 2711–2726.

Yang, Y., and X. Lee. 2019. "Four-band thermal mosaicking: A new method to process infrared thermal imagery of urban landscapes from UAV flights." *Remote Sensing* 11 (11): 1365.

Yuan, C., Y. Zhang, and Z. Liu. 2015. "A survey on technologies for automatic forest fire monitoring, detection, and fighting using unmanned aerial vehicles and remote sensing techniques." *Canadian journal of forest research* 45 (7): 783–792.